J. Fluid Mech. (2016), *vol.* 805, R1, doi:10.1017/jfm.2016.558

JFM RAPIDS
journals.cambridge.org/rapids

Multi-particle dispersion during entrainment in turbulent free-shear flows

Tomoaki Watanabe[1,†], **Carlos B. da Silva**[2] **and Koji Nagata**[1]

[1]Department of Aerospace Engineering, Nagoya University, Nagoya 464-8603, Japan

[2]IDMEC, Instituto Superior Técnico, Universidade de Lisboa, Lisboa 1049-001, Portugal

(Received 19 May 2016; revised 26 July 2016; accepted 18 August 2016;
first published online 16 September 2016)

Multi-particle dispersion is studied using direct numerical simulations of temporally evolving mixing layers and planar jets for tetrahedra consisting of four fluid particles which are seeded in the turbulent regions or in the non-turbulent regions near the turbulent/non-turbulent interface (TNTI). The modified Richardson law for decaying turbulence is observed for particle pairs. The size dependence of the mean and relative motions of the entrained tetrahedra indicates that the characteristic length scale of the entrained lumps of fluid is approximately 10 times the Kolmogorov microscale. When the tetrahedra move within the TNTI layer they are flattened and elongated by vortex stretching at a deformation rate that is characterized by the Kolmogorov time scale. The shape evolutions of the tetrahedra show that in free-shear flows, thin-slab structures of advected scalars are generated within the TNTI layers.

Key words: shear layers, turbulent flows, turbulent mixing

1. Introduction

Turbulent flows are often surrounded by non-turbulent (irrotational) fluid, the interface of which is a well-defined turbulent/non-turbulent interface (TNTI), where mass, momentum and energy exchanges occur, thereby allowing the growth of the turbulent region into the non-turbulent fluid. Thus, turbulence is often found to be localized, such as in the atmospheric boundary layer (Mahrt 1999) and the ocean mixing layer (Thorpe 1978). A TNTI is also found in canonical free-shear flows, such as jets, wakes and mixing layers, and these flows have been used frequently for studying TNTI mechanisms.

Corrsin & Kistler (1955) predicted the existence of a very thin 'viscous superlayer' (VSL) at the edge of the turbulence region, where the viscous diffusion of vorticity causes the spreading of turbulence (Taveira & da Silva 2014). This initial vorticity is matched between turbulent and non-turbulent flow regions in an adjacent

† Email address for correspondence: watanabe.tomoaki@c.nagoya-u.jp

© Cambridge University Press 2016

https://doi.org/10.1017/jfm.2016.558 Published online by Cambridge University Press

'turbulent sublayer' (TSL) region, located between the VSL and the turbulent core region (da Silva *et al.* 2014). Whereas the vorticity grows by viscous diffusion within the VSL, its growth is mainly governed by inviscid vortex stretching within the TSL (Taveira & da Silva 2014). The motions of entrained fluid particles are also different between the TSL and the VSL (Watanabe *et al.* 2016).

Lagrangian tracking of the fluid particles during the entrainment is useful for studying the entrainment process, and has been used in recent experiments and direct numerical simulations (DNS) (Holzner *et al.* 2008; Taveira *et al.* 2013; Watanabe *et al.* 2016). Virtually all of these studies only show one-particle statistics during the entrainment, which provide only information on one-point statistics along the entrained particle path line. Although the entrainment consists of a continuous transition of non-turbulent fluid into turbulence, resulting in the entrainment of an entire fluid volume, the evolution of material volume is not understood well in relation to the entrainment across the TNTI layer.

In contrast, a multi-particle dispersion analysis enables us to understand in detail the Lagrangian evolution of material lines, surfaces and volumes (Xu, Ouellette & Bodenschatz 2008). A fluid volume in three-dimensional space is defined by more than four different points. Therefore, the evolution of a fluid volume has been studied by tracking four-particle clusters (tetrahedra) (Pumir, Shraiman & Chertkov 2001; Xu *et al.* 2008; Schumacher 2009). The deformation of the fluid volume is related to the mixing mechanism of advected scalars; thin and long slabs of contaminant are formed by the deformation of fluid packets (Brethouwer, Hunt & Nieuwstadt 2003), enhancing molecular diffusion in regions of intense scalar gradient. The investigation of entrained fluid volumes thus provides much detailed information on the turbulent entrainment mechanism.

In this paper, new DNS are used to report on multi-particle dispersion statistics in temporally evolving mixing layers and planar jets. By tracking a number of tetrahedra, we investigate the kinetic energy evolution and deformation of fluid elements during the entrainment. The statistics of two-particle pairs are also used for examining the modified Richardson law proposed for decaying turbulence (Larcheveque & Lesieur 1981). The new results also provide a new challenging test ground for recent subgrid-scale Lagrangian turbulence models (e.g. Mazzitelli, Toschi & Lanotte 2014).

2. Direct numerical simulations of temporally evolving planar jets and mixing layers

2.1. *Numerical methods and computational parameters*

Direct numerical simulations are performed for temporally evolving mixing layers and planar jets (Watanabe *et al.* 2016). The computation domains with a size of $L_x \times L_y \times L_z$ are represented by $N_x \times N_y \times N_z$ grid points. The flows are periodic in the streamwise (x) and spanwise (z) directions, and spread in the cross-streamwise (y) direction, where slip boundary conditions are applied. The origin of the coordinate system is located at the centre of the computational domain. The DNS code is an incompressible Navier–Stokes solver based on the fractional step method, and was used in our previous studies (Watanabe & Nagata 2016; Watanabe *et al.* 2016). The governing equations are solved by using a fully conservative finite-difference method for spatial discretization and a third-order Runge–Kutta method for temporal advancement. Fourth-order and second-order central difference schemes are used in the periodic and cross-streamwise directions respectively. The Poisson equation for pressure is solved by using the Bi-CGSTAB method. For the mixing layers, a passive

https://doi.org/10.1017/jfm.2016.558 Published online by Cambridge University Press

Run	ML02	ML06	PJ10	PJ20
Flow type	Mixing layer	Mixing layer	Planar jet	Planar jet
Re	2000	6000	10 000	20 000
L_x, L_y, L_z	$42\theta_M$, $54\theta_M$, $28\theta_M$	$42\theta_M$, $54\theta_M$, $28\theta_M$	$6H$, $11H$, $4H$	$6H$, $11H$, $4H$
N_x, N_y, N_z	1200, 1400, 800	2700, 3000, 1800	1200, 1600, 800	1500, 2400, 1000
Time step dt	$0.02\theta_M/U_M$	$0.01\theta_M/U_M$	$0.0025H/U_J$	$0.002H/U_J$
$\Delta_x = \Delta_z, \Delta_y$	1.8η, 1.3η	1.8η, 1.4η	1.4η, 1.2η	1.8η, 1.4η
Re_λ	202	365	132	201
λ/η	28	38	23	27

TABLE 1. Physical and computational parameters of the DNS. The displayed turbulence characteristics are from the turbulent core regions when the particles are seeded.

scalar ϕ, whose evolution is described by the convection–diffusion equation with the Schmidt number $Sc = \nu/D = 1$, is also simulated as in Watanabe *et al.* (2015), where ν is the kinematic viscosity and D is the molecular diffusivity. The grid is equidistant in the x and z directions, while in the y direction, a fine grid is used near the centre of the mixing layers and planar jets. In addition to solving the Navier–Stokes equations, the fluid particles are simultaneously tracked using a third-order Runge–Kutta scheme for temporal advancement and the trilinear interpolation scheme as in previous Lagrangian studies (Schumacher 2009; Watanabe *et al.* 2016).

The simulations are initialized by statistically homogeneous and isotropic velocity fluctuations, which are superimposed onto the mean streamwise velocity given by $\langle U\rangle = 0.5U_M \tanh(2y/\theta_M)$ in mixing layers and $\langle U\rangle = 0.5U_J + 0.5U_J \tanh[(H - 2|y|)/4\theta_J]$ in planar jets. Here, U_M is the velocity difference in the mixing layers, U_J is the jet velocity, H is the width of the jet inlet and θ_M (θ_J) is the initial shear layer thickness in the mixing layers (planar jets). The angular bracket denotes the averaged value in an x–z plane. We set $\theta_J = 0.015H$. The initial scalar profile in the mixing layer is given by $\phi = 0.5\tanh(2y/\theta_M)$. The Reynolds numbers Re are defined by $U_M\theta_M/\nu$ and U_JH/ν. The DNS are performed for the planar jets at $Re = 10\,000$ and 20 000 and for the mixing layers at $Re = 2000$ and 6000. The physical and computational parameters are listed in table 1 (λ is the Taylor microscale, η is the Kolmogorov scale and Re_λ is the turbulent Reynolds number). As shown in table 1, the spatial resolutions, Δ_i, are small and comparable to the Kolmogorov scale on the centreline, and are therefore small enough to capture the small-scale fluctuations.

2.2. *Lagrangian particle tracking*

Once the mixing layers and planar jets have reached a self-similar state, we seed 40 000 tetrahedra consisting of four particles each and start to track $4 \times 40\,000$ particles. Two cases are considered in this study: (i) tetrahedra seeded inside the turbulent region and (ii) tetrahedra seeded in the non-turbulent region near the TNTI. The turbulent region is detected as the region with $|\boldsymbol{\omega}| > \omega_{th}$ (da Silva *et al.* 2014), where $|\boldsymbol{\omega}|$ is the magnitude of the vorticity vector, which is defined as the curl of the velocity field $\omega_i = \varepsilon_{ijk}\partial u_k/\partial x_j$. The threshold ω_{th} is determined so that the isosurface $|\boldsymbol{\omega}| = \omega_{th}$ is located near the outer edge of the TNTI layer using a well-known feature of the dependence of the turbulent volume on ω_{th} (Taveira *et al.* 2013). It has been shown that the interface boundary location computed using this procedure, as well as the resulting conditional statistics, is insensitive to the particular value of the ω_{th} thus obtained. In the present DNS, ω_{th} is 4 % of the mean vorticity magnitude on

https://doi.org/10.1017/jfm.2016.558 Published online by Cambridge University Press

the centreline (Watanabe *et al.* 2015). This isosurface is referred to as the irrotational boundary hereafter (Watanabe *et al.* 2015). The tetrahedra are seeded with the method used by Schumacher (2009) where an initial tetrahedron consists of four particles located at $\boldsymbol{x}_1 = \boldsymbol{x}_0$, $\boldsymbol{x}_2 = \boldsymbol{x}_0 + r_0\boldsymbol{e}_x$, $\boldsymbol{x}_3 = \boldsymbol{x}_0 + r_0\boldsymbol{e}_y$ and $\boldsymbol{x}_4 = \boldsymbol{x}_0 + r_0\boldsymbol{e}_z$ ($\boldsymbol{x}_3 = \boldsymbol{x}_0 - r_0\boldsymbol{e}_y$ is used when $y_0 < 0$), where $\boldsymbol{e}_i$ is the unit vector in the i direction. Here, $\boldsymbol{x}_0$ is randomly chosen from the turbulent region in the case (i) and from the non-turbulent region near the TNTI in the case (ii). When the tetrahedra are seeded inside the turbulent region, all particles of the tetrahedra are located inside the turbulent region, whereas in case (ii), all particle locations $\boldsymbol{x}_1$, $\boldsymbol{x}_2$, $\boldsymbol{x}_3$ and $\boldsymbol{x}_4$ are in the non-turbulent region. The simulations are performed for tetrahedra with initial side lengths of $r_0 = 2\eta$, 4η, 8η, 16η, 32η and 48η. We calculate two-particle statistics from the pairs of ($\boldsymbol{x}_1$, $\boldsymbol{x}_2$), ($\boldsymbol{x}_1$, $\boldsymbol{x}_3$) and ($\boldsymbol{x}_1$, $\boldsymbol{x}_4$), while the tetrahedra are used for four-particle statistics.

The Lagrangian multi-particle statistics are computed as a function of time τ from the above DNS results. In the case (i), τ is defined as the time after the particles are released. The case (ii) uses the time elapsed after one of the particles making pairs or tetrahedra crosses the irrotational boundary. We denote the ensemble average of pairs or tetrahedra by $\langle * \rangle_\tau$. The Lagrangian studies of the entrainment showed that the entrained fluid particles stay in the VSL for $0 \leqslant \tau \lesssim 7\tau_\eta$, and it takes more than $20\tau_\eta$ for the particles to cross the entire TNTI layer (Watanabe *et al.* 2016), where $\tau_\eta = (\nu/\varepsilon)^{1/2}$ is the Kolmogorov time scale (ε is the mean kinetic energy dissipation rate). In the present paper, the Lagrangian statistics are presented for large enough τ to observe the entrained particle movements in the entire TNTI layers. It has been confirmed that the small-scale characteristics of the entrainment are qualitatively similar in mixing layers and planar jets (Watanabe *et al.* 2016). Therefore, we discuss differences between the two flow types when the results are related to large-scale quantities.

3. Results and discussion

3.1. *Two-particle dispersion*

The relative location of two particles is described by the separation vector $\boldsymbol{R}(\tau) = \boldsymbol{x}_2(\tau) - \boldsymbol{x}_1(\tau)$. The classical Richardson scaling $\langle R^2 \rangle_\tau \sim \tau^3$ is only valid in statistically stationary flows. In non-stationary decaying turbulence, a modified Richardson law is obtained for the separation vector as (Larcheveque & Lesieur 1981)

$$\frac{\mathrm{d}\langle R^2(\tau)\rangle_\tau}{\mathrm{d}\tau} \sim \varepsilon^{1/3}(\tau)\langle R^2(\tau)\rangle_\tau^{2/3} \quad (\eta \ll |\boldsymbol{R}| \ll L), \tag{3.1}$$

where L is the integral scale and $\varepsilon(t)$ is the time-dependent mean kinetic energy dissipation rate. The classical scaling for the energy dissipation rate, $\varepsilon \sim u'^3/L$ (u' is the root mean square velocity), supports the power-law decay $\varepsilon(t) \sim t^{-n}$ in the self-similar regime of temporally evolving free-shear flows, where $n = 1$ in mixing layers and $n = 2$ in planar jets. The present DNS also confirmed these decay exponents. Integration of (3.1) with $\varepsilon(t) \sim t^{-n}$ yields

$$\langle R^2(\tau)\rangle_\tau = g_m \varepsilon(\tau)\tau^3, \tag{3.2}$$

where g_m is defined as the modified Richardson constant.

Figure 1(*a*,*b*) shows $\langle (R^2 - r_0^2)/\varepsilon \rangle_\tau^{1/3}/(r_0^2/\varepsilon_0)^{1/3}$ divided by τ/τ_η for particles released in the turbulent region and in the non-turbulent regions near the TNTI in PJ20, where

https://doi.org/10.1017/jfm.2016.558 Published online by Cambridge University Press

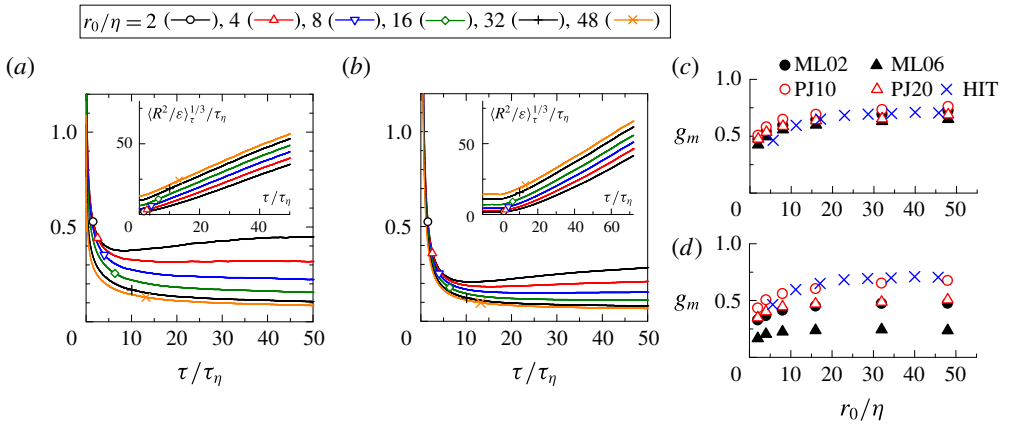

FIGURE 1. (*a*,*b*) Plots of $\langle (R^2 - r_0^2)/\varepsilon\rangle_\tau^{1/3}$ normalized by $(r_0^2/\varepsilon_0)^{1/3}$ (ε_0 is the kinetic energy dissipation rate at the centreline at the time when the particles are released) and compensated by τ/τ_η in PJ20 for two-particle pairs released (*a*) in the turbulent region and (*b*) in the non-turbulent region near the TNTI, with initial separations equal to $r_0/\eta = 2, 4, \ldots, 48$, where the Richardson-like scaling appears as a plateau. Here, r_0^2/ε_0 and τ_η used in the normalization are taken at the jet centreline at the time when the particles are released. The insets show $\langle R^2/\varepsilon\rangle_\tau^{1/3}$ against τ, where the Richardson-like scaling appears as a straight line. The symbols denote the time $(r_0^2/\varepsilon_0)^{1/3}$. (*c*,*d*) The modified Richardson constant g_m plotted against r_0/η for two-particle pairs released (*c*) in the turbulent region and (*d*) in the non-turbulent region near the TNTI. The Richardson constant g in forced homogeneous isotropic turbulence (HIT) (Ishihara & Kaneda 2002) is also shown for comparison.

ε_0 is the kinetic energy dissipation rate at the centreline at the time when the particles are released. Richardson-like scaling is expected to be observed for times larger than $(r_0^2/\varepsilon_0)^{1/3}$ (Bourgoin *et al.* 2006). According to studies on the relative dispersion in stationary turbulence (Ott & Mann 2000; Ishihara & Kaneda 2002), equation (3.2) is also examined by using the plot of $\langle R^2/\varepsilon\rangle_\tau^{1/3}$ against τ in the insets. Although the separation distance hardly changes before the particles cross the irrotational boundary ($\tau \leqslant 0$), the modified Richardson law (3.2) is satisfied in the turbulent core regions. The other jet and mixing layer simulations in the present study also yielded similar results. The modified Richardson constant is obtained by applying the least-squares method to $\langle R^2/\varepsilon\rangle_\tau^{1/3}$, and is plotted as a function of the initial separation r_0 in figure 1(*c*,*d*). For the particles released in the turbulent region, g_m increases slightly with increasing r_0 for small r_0, as in forced homogeneous isotropic turbulence. For $r_0/\eta \geqslant 32$, g_m hardly depends on the initial separation, and $g_m \approx 0.65$–0.75, with small variations with the Reynolds number and flow configuration. This value of g_m is very close to the Richardson constant in statistically stationary turbulence. For the entrained particle pairs, g_m shows a variation depending on the flow, and g_m decreases as Re_λ increases. It is found that the cases PJ20 and ML02, where $Re_\lambda \approx 200$, give similar values of g_m.

3.2. *Motions of tetrahedra*

We consider the motions of tetrahedra, which consist of four particles with the location $\boldsymbol{x}^{(n)}$ and the velocity $\boldsymbol{u}^{(n)}$ ($n = 1, \ldots, 4$). The kinetic energy of the motion

https://doi.org/10.1017/jfm.2016.558 Published online by Cambridge University Press

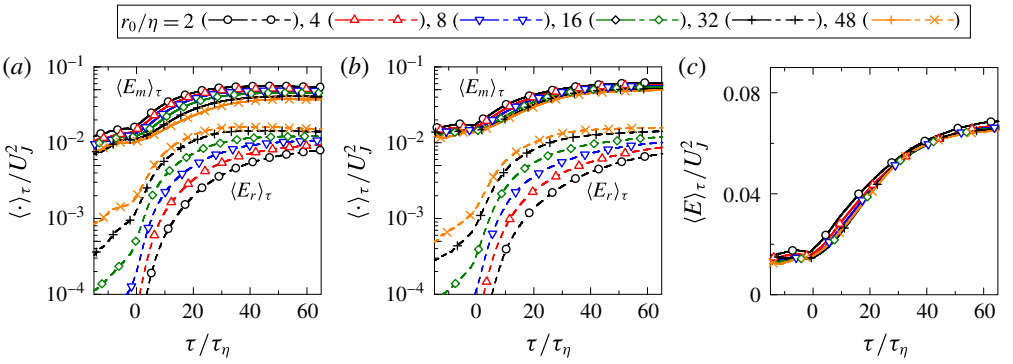

FIGURE 2. Averaged kinetic energy of mean (E_m) and relative (E_r) motions of tetrahedra during entrainment in planar jets: (*a*) PJ10 and (*b*) PJ20. (*c*) Averaged kinetic energy ($E = E_m + E_r$) in PJ20.

of a tetrahedron (Pumir *et al.* 2001) is defined by $E = \overline{(\boldsymbol{u}\cdot\boldsymbol{u})/2}$, where the overbar denotes the averaged value of the four particles of a tetrahedron. Since the velocity of the particle relative to the centre-of-mass motion is given by $\boldsymbol{u}'^{(n)} = \boldsymbol{u}^{(n)} - \overline{\boldsymbol{u}}$, the kinetic energy of the particle motion can be rewritten as $E = E_m + E_r$, where $E_m = (\overline{\boldsymbol{u}}\cdot\overline{\boldsymbol{u}})/2$ and $E_r = \overline{(\boldsymbol{u}'\cdot\boldsymbol{u}')}/2$ are the kinetic energies of the mean and relative motions respectively. Figure 2(*a*,*b*) shows the averaged energies of the mean and relative motions of tetrahedra during the entrainment in the planar jets. For both values of Re, the kinetic energy of the tetrahedra evolves similarly with time. Once a part of the tetrahedron crosses the irrotational boundary, both $\langle E_m\rangle_\tau$ and $\langle E_r\rangle_\tau$ increase rapidly, while they show a slower increase in the non-turbulent region. For a tetrahedron with a larger initial size, the relative motions have larger kinetic energy. However, when the total kinetic energy $\langle E\rangle_\tau$ is plotted as in figure 2(*c*), the dependence on the initial size is hardly seen during the entrainment. Thus, in the planar jets, although the tetrahedra gain kinetic energy almost independent of their initial size, their size affects the ratio between the mean and relative kinetic energy. The relative particle motions are mainly associated with the small scales of motion, and are therefore relatively flow-independent. Thus, the growth rate of the energy in the relative motions during entrainment is similar in jets and mixing layers. However, the energy of the mean motions is flow-dependent because of the different mean velocity profiles; in the temporal mixing layers, $\langle E_m\rangle_\tau$ rapidly decreases during the entrainment.

The equations governing the kinetic energy of the mean and relative motions of a tetrahedron are written as

$$\frac{\mathrm{d}E_m}{\mathrm{d}t} = -\overline{u_j}\frac{\overline{\partial p}}{\partial x_j} + 2\nu\frac{\partial \overline{u_i}\,\overline{S_{ij}}}{\partial x_j} - 2\nu\overline{S_{ij}}\,\overline{S_{ij}} = D_{pm} + D_{vm} + \varepsilon_m, \tag{3.3}$$

$$\frac{\mathrm{d}E_r}{\mathrm{d}t} = -\overline{u_j'\frac{\partial p'}{\partial x_j}} + 2\nu\frac{\partial \overline{u_i'S_{ij}'}}{\partial x_j} - 2\nu\overline{S_{ij}'S_{ij}'} = D_{pr} + D_{vr} + \varepsilon_r, \tag{3.4}$$

where p is the pressure divided by the constant density and S_{ij} is the strain tensor. The first, second and third terms are the pressure diffusion, viscous diffusion and dissipation terms respectively. Figure 3(*a*) compares $\langle \mathrm{d}E_m/\mathrm{d}t\rangle_\tau$ and $\langle \mathrm{d}E_r/\mathrm{d}t\rangle_\tau$ among different initial sizes of the tetrahedra released in the non-turbulent region for PJ20.

https://doi.org/10.1017/jfm.2016.558 Published online by Cambridge University Press

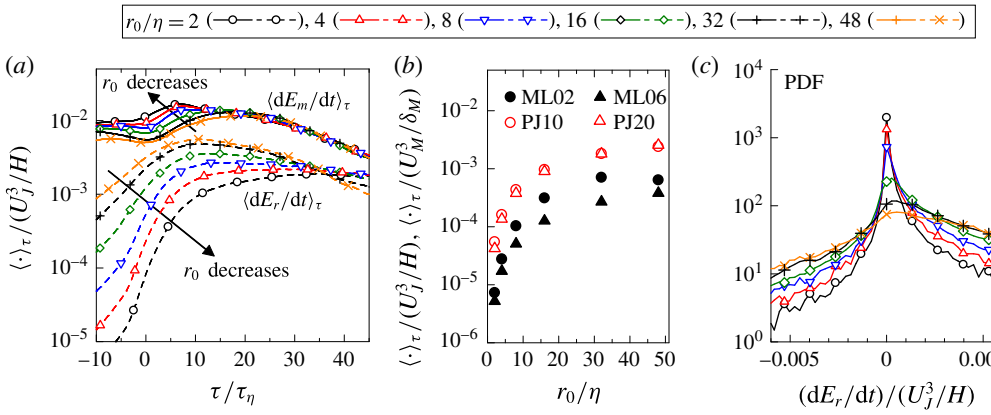

FIGURE 3. (*a*) Averaged growth rates of the kinetic energies of the mean and relative motions of tetrahedra during entrainment in a planar jet (PJ20). (*b*) Dependence of $\langle dE_r/dt\rangle_\tau$ at $\tau = 0$ on the initial size of the tetrahedra. (*c*) The PDF of dE_r/dt for PJ20 at $\tau = 14\tau_\eta$.

The tetrahedra gain more energy in relative motions for larger initial sizes. For $r_0/\eta \geqslant 16$, $\langle dE_r/dt\rangle_\tau$ has a peak value around $\tau \approx 10\tau_\eta$, at which more than one particle is passing the TNTI layer (Watanabe *et al.* 2016), and the relative motions grow rapidly during the entrainment process. For small tetrahedra, the growth rate of the relative motions is kept low in the TNTI layer. This is highlighted in figure 3(*b*), where $\langle dE_r/dt\rangle_\tau$ at $\tau = 0$ is plotted against r_0 for all DNS. Moreover, it is found that $\langle dE_r/dt\rangle_\tau$ is significantly decreased as r_0 becomes small for $r_0 \lesssim 10\eta$. Indeed, figure 3(*c*) shows the probability density functions (PDFs) of dE_r/dt during the entrainment of tetrahedra in PJ20. These PDFs display a large peak at $dE_r/dt = 0$ for $r_0 \lesssim 10\eta$, and this peak significantly decreases from $r_0 = 8\eta$ to 32η. Since these PDFs are positively skewed and the relative motion grows during the entrainment process, the statistics of dE_r/dt imply that the four-particle cluster being entrained crosses the TNTI layer nearly along with the motion of the mass centre when the length scale of the volume defined by the particles is less than $\sim 10\eta$.

Figure 4(*a*) shows the average of each term in (3.3) for two initial sizes of the tetrahedra. The tetrahedra being entrained gain the kinetic energy of the mean motions by the pressure diffusion. Even in the non-turbulent region, the kinetic energy of the mean motions is increased by the pressure diffusion. The growth rate of the energy of the mean motions becomes large when the tetrahedra are passing the TNTI ($\tau \approx 10\tau_\eta$), which is consistent with a mean velocity jump observed in the TNTI layer (Westerweel *et al.* 2009). Unlike what is observed in planar jets, the energy of the mean motions in mixing layers is reduced during the entrainment because of differences in the mean velocity profiles (not shown). However, we observed that the pressure diffusion dominates the mean motion in both mixing layers and jets. Figure 4(*b*,*c*) shows the average of each term in (3.4). For small tetrahedra with $r_0 = 2\eta$, the initial growth of the relative motions is caused by the viscous diffusion, D_{vr}. For larger tetrahedra, the pressure diffusion has a non-negligible contribution to the energy of relative motion even in the non-turbulent region. The pressure effects on the large tetrahedra cause rapid growth of the energy of relative motions during the entrainment.

The decomposition $\boldsymbol{u}^{(n)} = \overline{\boldsymbol{u}} + \boldsymbol{u}'^{(n)}$ can be considered as a scale decomposition: the large-scale velocity $\overline{\boldsymbol{u}}$ by a low-pass filtering and the small-scale velocity $\boldsymbol{u}'$

https://doi.org/10.1017/jfm.2016.558 Published online by Cambridge University Press

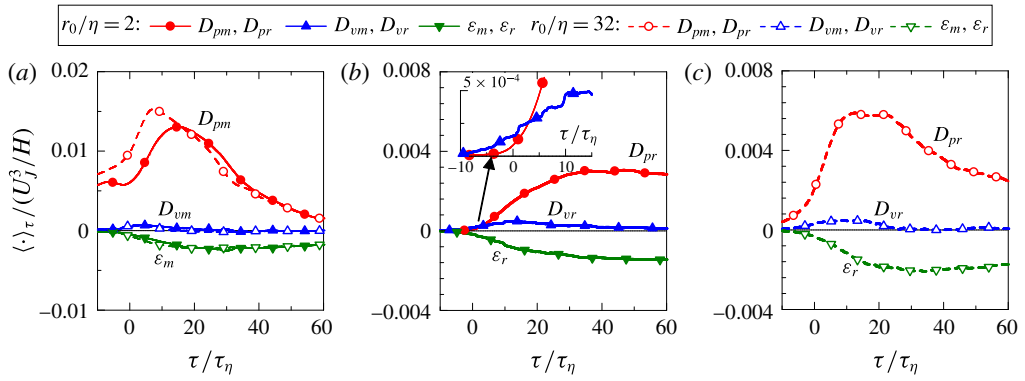

FIGURE 4. (*a*) Averaged budget of kinetic energy for the mean motion (3.3) for the initial sizes $r_0/\eta = 2$ and 32 in PJ20. (*b*,*c*) Averaged budget of kinetic energy for the relative motion (3.4) for (*b*) $r_0/\eta = 2$ and (*c*) $r_0/\eta = 32$. The inset in (*b*) shows the profiles around $\tau = 0$.

by a high-pass filtering (Pumir *et al.* 2001). Then, the r_0 dependence of $\mathrm{d}E_r/\mathrm{d}t$ implies the scale dependence of the kinetic energy transfer. Since the volume of the tetrahedra hardly changes at $\tau \lesssim 0$, the initial length r_0 can be used as the length of the scale decomposition, and E_r represents the kinetic energy contained in the scales smaller than r_0. Thus, the kinetic energy at small scales (E_r with small r_0) grows by the viscous diffusion, while as r_0 increases the pressure diffusion becomes dominant. In the Eulerian kinetic energy budget, the pressure diffusion was also found to be important in the energy transfer near the TNTI (Taveira & da Silva 2013). Furthermore, the mean and relative motions of tetrahedra provide the scale dependence of this energy transfer in the fluid motions. The r_0 dependence of D_{pr} indicates that most energy transferred by the pressure diffusion is contained in scales larger than $\sim 10\eta$. This is likely to be caused by the presence of coherent eddy motions near the interface, with length scales of the order of $\sim 10\eta$, since these structures display a pressure minimum that is long lived and thus able to imprint long-lasting effects on the nearby particle dynamics. The tetrahedra in the non-turbulent regions have non-trivial mean kinetic energy, whereas relative motions are absent especially for small tetrahedra. This can be related to the large-scale irrotational motions, which were also observed in the Eulerian statistics in planar jets (da Silva & Pereira 2008).

3.3. *Shape evolution of tetrahedra*

The shape of tetrahedra is well described by the position of the particles relative to the centre position $\boldsymbol{r}^{(n)} = \boldsymbol{x}^{(n)} - \bar{\boldsymbol{x}}$. The volumetric tensor (Robert *et al.* 1998) is defined by $R_{ij} = \overline{r_i r_j}$, and has three eigenvalues denoted by R_1, R_2 and R_3, ranging from the largest to the smallest ($R_1 \geqslant R_2 \geqslant R_3$); the corresponding eigenvectors are $\boldsymbol{e}_1$, $\boldsymbol{e}_2$ and $\boldsymbol{e}_3$. Three parameters can be defined by the eigenvalues of the volumetric tensor (Robert *et al.* 1998). One is the characteristic size of the tetrahedron: $L = 2\sqrt{R_1}$. The shape is described by the other two parameters: elongation E and planarity P, defined by $E = 1 - \sqrt{R_2/R_1}$ and $P = 1 - \sqrt{R_3/R_2}$. When four particles lie nearly on a straight line, $R_2 \approx R_3 \approx 0$, resulting in $E \approx 1$, and the direction of elongation is given by $\boldsymbol{e}_1$. When a tetrahedron is squashed in one direction and four particles lie nearly on a plane,

https://doi.org/10.1017/jfm.2016.558 Published online by Cambridge University Press

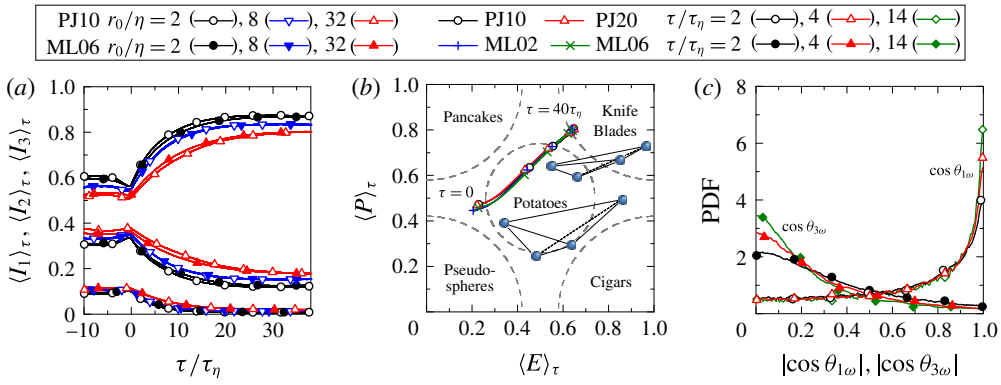

FIGURE 5. (*a*) Mean normalized eigenvalues of the moment-of-inertia tensor during entrainment in a mixing layer (ML06) and a planar jet (PJ10). (*b*) Averaged shape evolutions of tetrahedra with $r_0 = 2\eta$ across the TNTI on the E–P map. Examples of potatoes ($P = 0.52$, $E = 0.6$) and knife blades ($P = 0.84$, $E = 0.82$) are also shown in the figure. Tetrahedron shapes are characterized by elongation E and planarity P (Robert *et al.* 1998). Symbols mark the specific times of $\tau/\tau_\eta = 0$, 5, 10, 20 and 40. (*c*) The PDFs of the cosines of the angles between the vorticity vector ($\boldsymbol{\omega}$) and the elongation and planarity-normal directions ($\boldsymbol{e}_1$, $\boldsymbol{e}_3$). The PDF is shown for the tetrahedra being entrained with $r_0/\eta = 2$ at $\tau/\tau_\eta = 2$, 4 and 14 in ML02.

$R_2 \gg R_3$ and $P \approx 1$, and the normal of the planarity is given by $\boldsymbol{e}_3$. The volumetric tensor is also related to the moment-of-inertia tensor, and the normalized eigenvalues of the moment-of-inertia tensor are obtained by $I_i = R_i/(R_1 + R_2 + R_3)$.

Figure 5(*a*) shows $\langle I_i\rangle_\tau$ during the entrainment in PJ10 and ML06, which have the smallest and the largest Re_λ in the present DNS datasets respectively. Once the tetrahedra cross the irrotational boundary, they rapidly deform while passing the TNTI layers. The time scale of the deformation is very similar for $r_0/\eta = 2$ and 8 in both PJ10 and ML06, and scales with the Kolmogorov time scale $\tau_\eta = (\nu/\varepsilon)^{1/2}$, indicating that the local strain rate, of order $(\varepsilon/\nu)^{1/2}$, dominates the deformation. The mean values of I_i for large τ become close to those observed in other flows (Schumacher 2009). Figure 5(*b*) shows the mean trajectory on the E–P map after a part of a tetrahedron crosses the irrotational boundary. Once the tetrahedron moves within the TNTI layer, the shape changes into a knife-blade shape, which is both elongated and flattened, and a tetrahedron with $r_0/\eta = 2$ reaches a quasi-stationary shape $(E, P) = (0.62, 0.80)$ at $\tau = 20\tau_\eta$, at which the particles are located in the TSL (Watanabe *et al.* 2016). This shape evolution is very similar in planar jets and mixing layers.

Figure 5(*c*) shows the PDFs of $|\cos\theta_{1\omega}|$ and $|\cos\theta_{3\omega}|$, where $\theta_{i\omega}$ is the angle between $\boldsymbol{e}_i$ and $\boldsymbol{\omega}$ at one of the four particle locations ($\boldsymbol{x}_1$). The PDF shows that the direction of elongation ($\boldsymbol{e}_1$) tends to align with $\boldsymbol{\omega}$, and the tetrahedron is flattened in the direction perpendicular to $\boldsymbol{\omega}$. This indicates that the vortical structures are circulated around by the entrained tetrahedra which are elongated in the direction of $\boldsymbol{\omega}$. The elongation in the vorticity direction can be related to the strain field stretching the vorticity vector. As shown from the deformation time scale, the entrained fluid volume is deformed by the local strain $S' \sim (\varepsilon/\nu)^{1/2}$, which acts on the small-scale eddy structures, whose radius sizes are 4–5η (da Silva, Dos Reis & Pereira 2011). Thus, the elongation of

https://doi.org/10.1017/jfm.2016.558 Published online by Cambridge University Press

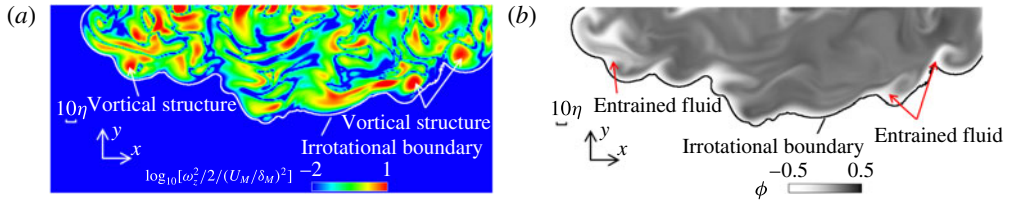

FIGURE 6. Visualization of (*a*) the spanwise vorticity squared, ω_z^2, and (*b*) the scalar ϕ near the TNTI in ML06. The irrotational boundary, $|\boldsymbol{\omega}| = \omega_{th}$, is shown by a thin line. The vortical structures with large ω_z are marked in (*a*), while the entrained fluid around the spanwise vortical structures is marked in (*b*).

the fluid volume during the entrainment is related to the small-scale eddies, which are sustained by the strain S' within the TSL.

The growth rate of the energy of the relative motions clearly changes around $r_0 \approx 10\eta$, as shown in figure 3. Considering the small energy in the relative motions for $r_0 \leqslant 10\eta$ during the entrainment (figure 2), we can anticipate that a lump of non-turbulent fluid with a size of approximately 10η is entrained undergoing the deformation by the local strain acting on the small-scale eddy in the TSL, resulting in the thin-slab structures of the entrained fluid. Figure 6 confirms this shape evolution of the small entrained fluid volume. Along a fluid particle, ϕ changes only by molecular diffusion. Therefore, the entrained fluid near the TNTI has ϕ close to non-turbulent values (Watanabe *et al.* 2015). In figure 6(*a*), we can see that the spanwise vortical structures with large ω_z have a core radius of approximately 5η, like the intense vorticity structures studied by da Silva *et al.* (2011). In figure 6(*b*), thin-slab structures of the entrained fluid with $\phi \approx -0.5$ (white) are found around the vortical structures with large ω_z, and are flattened so that the planarity normal is perpendicular to the vorticity vector (z) direction. This result agrees with the previous Lagrangian statistics, showing that the entrained fluid circumvents the strong-vorticity regions near the TNTI (Watanabe *et al.* 2016). In figure 6(*b*), the size of the entrained thin-slab structures is comparable to the vortical structures ($\sim$5–10η), as expected from the small kinetic energy of the relative motion of entrained tetrahedra with $r_0 \leqslant 10\eta$. Thus, some of the thin-slab structures observed in free-shear flows are formed during the entrainment process. It should be noted that this generation process of thin-slab structures inside fully developed turbulence (Brethouwer *et al.* 2003) is also possible in the thin shear layer between intense and weak turbulent regions, which was observed in high-*Re* turbulent flows (Ishihara, Kaneda & Hunt 2013).

4. Conclusions

Multi-particle dispersion is investigated in the self-similar regimes of temporally evolving mixing layers and planar jets. Tetrahedra consisting of four particles are seeded in the turbulent and non-turbulent regions near the TNTI. The modified Richardson law proposed for decaying isotropic turbulence (Larcheveque & Lesieur 1981) is also observed within the turbulent regions of the mixing layers and planar jets, although with a modified Richardson constant $g_m \approx 0.65$–0.75 for two-particle pairs released in the turbulent region. For particle pairs being entrained, g_m is largely *Re*-dependent in both flows.

https://doi.org/10.1017/jfm.2016.558 Published online by Cambridge University Press

When four-particle clusters are entrained, both the mean and the relative motions of the particles in relation to the centre of mass, as well as their geometry, rapidly change within the TNTI layers. Interestingly, the size of the entrained lumps of fluid largely impacts on the associated kinetic energy evolution within the TNTI. While the typical size of the entrained lumps of fluid is $\sim 10\eta$, the kinetic energy of the relative motions increases faster for larger tetrahedra. The mean kinetic energy of the entraining particle cluster is mainly caused by pressure–velocity interactions associated with the large scales, while the relative motion of smaller tetrahedra is mainly caused by small-scale viscous effects at the initial stage of the entrainment. Moreover, when the length scale of the tetrahedra is smaller than approximately 10η, the entraining particles tend to move along with the mean motion trajectories. Once a part of the tetrahedron moves into the TNTI layer, it starts to rapidly deform until it becomes of an elongated and flattened shape, and the associated time scale of this deformation is of the order of the Kolmogorov time scale. During the entrainment, the fluid elements are elongated in the vorticity direction near the TNTI.

These results describe the entrainment as follows: (i) a fluid volume with a size of approximately 10η is entrained as a lump of fluid, (ii) the lump of fluid is deformed by local strain acting on small-scale eddies within the TSL and (iii) it deforms into thin-slab structures consisting of the original entrained fluid packet. The present results provide insightful new information that could be used in the development of subgrid-scale Lagrangian turbulence models (e.g. Mazzitelli *et al.* 2014).

Acknowledgements

The numerical simulations presented in this paper were carried out on the high-performance computing system (NEC SX-ACE) at the Japan Agency for Marine–Earth Science and Technology. This work was partially supported by 'Collaborative Research Project on Computer Science with High-Performance Computing in Nagoya University'. This work was supported by JSPS KAKENHI grant numbers 25289030 and 16K18013. C.B.dS. acknowledges IDMEC, under LAETA projects PTDC/EME-MFE/122849/2010 and UID/EMS/50022/2013.

References

BOURGOIN, M., OUELLETTE, N. T., XU, H., BERG, J. & BODENSCHATZ, E. 2006 The role of pair dispersion in turbulent flow. *Science* **311** (5762), 835–838.

BRETHOUWER, G., HUNT, J. C. R. & NIEUWSTADT, F. T. M. 2003 Micro-structure and Lagrangian statistics of the scalar field with a mean gradient in isotropic turbulence. *J. Fluid Mech.* **474**, 193–225.

CORRSIN, S. & KISTLER, A. L. 1955 Free-stream boundaries of turbulent flows. *NACA Tech. Rep. No.* TN-1244.

HOLZNER, M., LIBERZON, A., NIKITIN, N., LÜTHI, B., KINZELBACH, W. & TSINOBER, A. 2008 A Lagrangian investigation of the small-scale features of turbulent entrainment through particle tracking and direct numerical simulation. *J. Fluid Mech.* **598**, 465–475.

ISHIHARA, T. & KANEDA, Y. 2002 Relative diffusion of a pair of fluid particles in the inertial subrange of turbulence. *Phys. Fluids* **14** (11), L69–L72.

ISHIHARA, T., KANEDA, Y. & HUNT, J. C. R. 2013 Thin shear layers in high Reynolds number turbulence – DNS results. *Flow Turbul. Combust.* **91** (4), 895–929.

LARCHEVEQUE, M. & LESIEUR, M. 1981 The application of eddy-damped Markovian closures to the problem of dispersion of particle pairs. *J. Méc.* **20** (1), 113–134.

MAHRT, L. 1999 Stratified atmospheric boundary layers. *Boundary-Layer Meteorol.* **90** (3), 375–396.

MAZZITELLI, I. M., TOSCHI, F. & LANOTTE, A. S. 2014 An accurate and efficient Lagrangian sub-grid model. *Phys. Fluids* **26** (9), 095101.

https://doi.org/10.1017/jfm.2016.558 Published online by Cambridge University Press

OTT, S. & MANN, J. 2000 An experimental investigation of the relative diffusion of particle pairs in three-dimensional turbulent flow. *J. Fluid Mech.* **422**, 207–223.

PUMIR, A., SHRAIMAN, B. I. & CHERTKOV, M. 2001 The Lagrangian view of energy transfer in turbulent flow. *Europhys. Lett.* **56** (3), 379–385.

ROBERT, P., ROUX, A., HARVEY, C. C., DUNLOP, M. W., DALY, P. W. & GLASSMEIER, K. H. 1998 Tetrahedron geometric factors. *Anal. Meth. Multi-Spacecraft Data* 323–348.

SCHUMACHER, J. 2009 Lagrangian studies in convective turbulence. *Phys. Rev.* E **79** (5), 056301.

DA SILVA, C. B., DOS REIS, R. J. N. & PEREIRA, J. C. F. 2011 The intense vorticity structures near the turbulent/non-turbulent interface in a jet. *J. Fluid Mech.* **685**, 165–190.

DA SILVA, C. B., HUNT, J. C. R., EAMES, I. & WESTERWEEL, J. 2014 Interfacial layers between regions of different turbulence intensity. *Annu. Rev. Fluid Mech.* **46**, 567–590.

DA SILVA, C. B. & PEREIRA, J. C. F. 2008 Invariants of the velocity-gradient, rate-of-strain, and rate-of-rotation tensors across the turbulent/nonturbulent interface in jets. *Phys. Fluids* **20** (5), 055101.

TAVEIRA, R. R., DIOGO, J. S., LOPES, D. C. & DA SILVA, C. B. 2013 Lagrangian statistics across the turbulent–nonturbulent interface in a turbulent plane jet. *Phys. Rev.* E **88** (4), 043001.

TAVEIRA, R. R. & DA SILVA, C. B. 2013 Kinetic energy budgets near the turbulent/nonturbulent interface in jets. *Phys. Fluids* **25**, 015114.

TAVEIRA, R. R. & DA SILVA, C. B. 2014 Characteristics of the viscous superlayer in shear free turbulence and in planar turbulent jets. *Phys. Fluids* **26** (2), 021702.

THORPE, S. A. 1978 The near-surface ocean mixing layer in stable heating conditions. *J. Geophys. Res.* **83** (C6), 2875–2885.

WATANABE, T. & NAGATA, K. 2016 Mixing model with multi-particle interactions for Lagrangian simulations of turbulent mixing. *Phys. Fluids* **28** (8), 085103.

WATANABE, T., SAKAI, Y., NAGATA, K., ITO, Y. & HAYASE, T. 2015 Turbulent mixing of passive scalar near turbulent and non-turbulent interface in mixing layers. *Phys. Fluids* **27** (8), 085109.

WATANABE, T., DA SILVA, C. B., SAKAI, Y., NAGATA, K. & HAYASE, T. 2016 Lagrangian properties of the entrainment across turbulent/non-turbulent interface layers. *Phys. Fluids* **28** (3), 031701.

WESTERWEEL, J., FUKUSHIMA, C., PEDERSEN, J. M. & HUNT, J. C. R. 2009 Momentum and scalar transport at the turbulent/non-turbulent interface of a jet. *J. Fluid Mech.* **631**, 199–230.

XU, H., OUELLETTE, N. T. & BODENSCHATZ, E. 2008 Evolution of geometric structures in intense turbulence. *New J. Phys.* **10** (1), 013012.

https://doi.org/10.1017/jfm.2016.558 Published online by Cambridge University Press